Journal of Materials Chemistry A

Proton-enabled biomimetic stabilization of small-molecule organic cathode in aqueous zinc-ion batteries

Journal:	*Journal of Materials Chemistry A*
Manuscript ID	TA-ART-03-2022-001621.R1
Article Type:	Paper
Date Submitted by the Author:	20-Apr-2022
Complete List of Authors:	Luu, Nhu; National Cheng Kung University College of Engineering, Chemical Engineering; National Cheng Kung University, Hierarchical Green-Energy Materials Research Center Ivanov, Alexander; Oak Ridge National Laboratory, Chemical Sciences Division Chen, Teng-Hao; National Cheng Kung University, Pharmacy Popovs, Ilja; Oak Ridge National Laboratory, Lee, Jui-Chin ; National Cheng Kung University, Core Facility Center Kaveevivitchai, Watchareeya; National Cheng Kung University, Chemical Engineering; National Cheng Kung University, Hierarchical Green-Energy Materials Research Center

ARTICLE

Proton-enabled biomimetic stabilization of small-molecule organic cathode in aqueous zinc-ion batteries

Received 00th January 20xx,
Accepted 00th January 20xx

DOI: 10.1039/x0xx00000x

Nhu T. H. Luu,[a] Alexander S. Ivanov,*[b] Teng-Hao Chen,[c] Ilja Popovs,[b] Jui-Chin Lee[d] and Watchareeya Kaveevivitchai*[a]

Small-molecule organic cathode materials offer flexible structural design features, high capacity and sustainable production. Nonetheless, stability decrease due to high solubility of the electrode materials especially upon electrochemical cycling conditions limits their wide-range applications in energy storage technologies. We describe nature-inspired strategy to address cathode stability via introduction of transient vinylogous amide hydrogen bond networks in the small-molecule organic electrode material—hexaazatrianthranylene (HATA) embedded quinone (HATAQ). Thanks to the proton-enabled biomimetic mechanism, HATAQ exhibits unparalleled cycling stability, ultra-high capacity and rate capability in the aqueous zinc-ion batteries, delivering 492 mAh g^{-1} at 50 mA g^{-1} and a reversible capacity of 199 mAh g^{-1}, corresponding to 99 % retention at 20 A g^{-1} after 1000 cycles.

Introduction

The development of reliable and sustainable large-scale electrochemical energy storage is urgently needed to take full advantage of ever-increasing availability of renewable energy and to ensure rapid decarbonization of global economy.[1] Aqueous zinc-ion batteries (AZIBs) could fill this gap if suitable cathode materials could be identified. Zinc metal is naturally abundant, inexpensive, non-toxic and, most importantly, compatible with water; therefore, it is a desirable anode for aqueous systems.[2] In the pursuit of cathode materials to couple with zinc anode, inorganic compounds such as manganese dioxides, vanadium oxides, Prussian blue analogues and polyanion compounds have been investigated.[3] However, large structural deformation due to insertion/extraction of guest species, strong electrostatic interactions with rigid host lattice and material dissolution generally lead to capacity fading and limited cycle life.[3]

Organic small molecule cathode (OSMC) materials have emerged as a viable alternative. Compared to inorganic cathodes, organic electrode materials are more flexible at accommodating guest ions, especially those divalent charge carriers (e.g., Zn^{2+} and Mg^{2+}).[4] Various organic functional groups such as carbonyl and amino groups can interact with guest ions via reversible coordination reaction; therefore, organic compounds can store these charged species. Apart from low toxicity, abundant resources, ease of synthesis and processing as well as recyclability of organic materials in comparison to inorganic electrodes, molecular design flexibility and structural tunability allow systematic adjustments of properties such as specific capacity (by adding redox-active functional groups), redox potential (by using electron-withdrawing or electron-donating groups), conductivity, redox kinetics and cycling stability of organic compounds.[4,5] Weak intermolecular interactions found in organic-based materials (e.g., π–π stacking, van der Waals forces and hydrogen bonding) are known to allow flexible structures and tunable intermolecular space which leads to a modest Coulombic attraction/repulsion between the soft host lattice and the guest charged species, thus offering energetically favorable migration pathways.[4,5]

However, frequent material dissolution in electrolytes along with the decrease in electron conductivity and ion mobility upon cycling are perhaps major issues plaguing OSMCs and preventing them from wider adoption.[5-7] While several strategies exist to improve their stability, such as salting[8] and polymerization,[9] these can lead to inferior rate capabilities and capacities due to unproductive increase of the equivalent molecular weight of electroactive material.[5] In addition to the strict requirements of molecular structure and the presence of electrochemically-active groups, electronic and ionic conductivity as well as structural stability are equally important.[10] Rationally designed cathode materials satisfying all these criteria are only beginning to emerge.[11] In contrast, nature has already developed essential toolkits for the complex hierarchical design and stabilization of three-dimensionally ordered supramolecules by balancing the strengths of multiple intra- and intermolecular noncovalent interactions, including examples of protein folding,[12] the formation of secondary

[a] Department of Chemical Engineering, National Cheng Kung University, Tainan City 70101, Taiwan; Hierarchical Green-Energy Materials Research Centre, National Cheng Kung University, Tainan City 70101, Taiwan.
[b] Chemical Sciences Division, Oak Ridge National Laboratory, Oak Ridge, P.O. Box 2008, TN 37831, USA.
[c] School of Pharmacy, National Cheng Kung University, Tainan City 70101, Taiwan.
[d] Core Facility Centre, National Cheng Kung University, Tainan City 70101, Taiwan.
† Electronic supplementary information (ESI) available: Detailed experimental procedures as well as additional computational and mechanistic data. For ESI or other electronic format, see DOI: 10.1039/x0xx00000x

structure[13] and enzymatic reactions, allowing the transfer of protons along specifically preorganized trajectories.[14]

Taking cues from nature, here we demonstrate a biomimetic stabilization strategy of hexaazatrianthranylene (HATA) embedded quinone (HATAQ) organic cathode (Fig. 1) by exploiting the formation of vinylogous amide group and transient hydrogen bond networks in the presence of aqueous proton source. Proton intercalation upon discharge gradually increases the number of hydrogen bonds that stabilize the structure of the discharged material in the solid state and creates favorable pathways for fast proton transfer, resulting in an unparalleled performance in AZIBs.

Results and discussion

According to our previous X-ray single-crystal and powder diffraction (PXRD) studies,[5] HATAQ exhibits a graphite-like 2D layered arrangement with multiple unconventional C-H···O interactions between HATAQ molecules, akin to those found in proteins.[15] Although regarded as weak, these hydrogen bonds along with π-π stackings seem to be responsible for the peculiar HATAQ supramolecular packing in the solid state.[5] To gain real-space insights into both long-range ordered structure and short-range structural correlations in the HATAQ material, we performed synchrotron X-ray scattering measurements at the National Synchrotron Light Source II (Fig. S1, S2, see ESI†). The obtained pair distribution function (PDF), G(r), that is related to the probability of finding atomic pairs with a given separation distance r, shows characteristic features consistent with the graphitic carbon materials.[16] The first three peaks in the PDF appear at distances of 1.42 (A), 2.44 (B) and 2.82 Å (C), which correspond to the in-plane distances in the aromatic rings (Fig. 1). There is also a less intense peak at ~2 Å, which could likely be attributed to C-H···O interactions, as follows from the partial radial distribution function for the H-O atomic pair correlation in an ideal periodic HATAQ structure (Fig. S3). The feature at ~3.4 Å, which is also seen in the simulated PDF, is due to the interlayer correlations, whereas the fourth intense peak in the experimental PDF appearing at 3.75 Å signifies in-plane C-C bond distances, similar to that found in graphite.[17] As seen in Fig. 1, the PDF signal exhibits damping behavior at longer r, indicating the average structural coherence length of ~12 Å in the HATAQ material that corresponds to the presence of nanocrystalline domains with the approximate size of 2 nm in diameter. In general, the high-energy X-ray scattering experiments suggest that the material is made of 2D layers of HATAQ molecules, which are spatially correlated on a nanoscale.

Having confirmed the outstanding stabilization effect of protic media (Fig. S4, S5) on the cathode material, we performed additional electrochemical studies using HATAQ as cathode with Zn metal as anode and 1 M $ZnSO_4$ aqueous solution as electrolyte, a more affordable alternative to $Zn(CF_3SO_3)_2$. The discharge/charge profiles and cycling performance at different current densities are shown in Fig. 2. Zn/HATAQ cells deliver remarkably high initial capacities of 492, 394 and 340 mAh g^{-1} at rates of 50, 200 and 500 mA g^{-1}, respectively. This highest capacity of 492 mAh g^{-1} (energy density

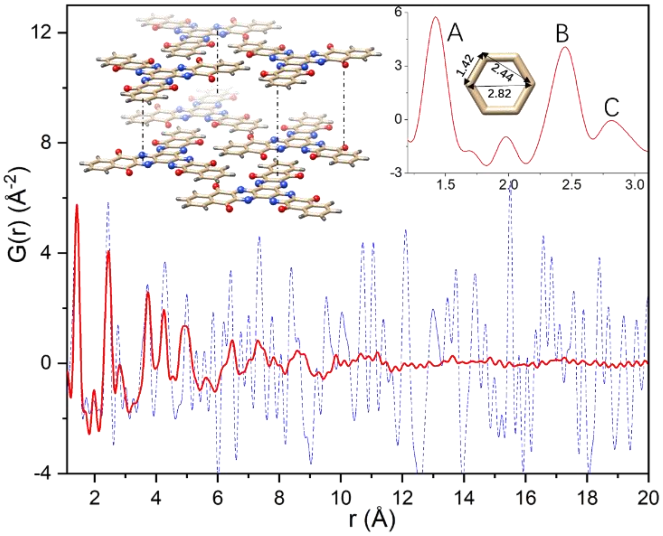

Fig. 1 Structure and atomic pair distribution function (PDF) of HATAQ (red line). Simulated PDF from an ideal periodic HATAQ structure (blue line) is given for comparison. The inset shows magnified region of the PDF data corresponding to the short-range structural correlations in HATAQ.

estimated to 344 Wh kg^{-1} with respect to cathode material) is close to HATAQ theoretical capacity of 516 mAh g^{-1} corresponding to 12-electron transfer. The voltage profiles (Fig. 2a) show several short plateaus, consistent with the main peak positions in the cyclic voltammogram (CV) in Fig. S26, which can be attributed to reversible redox reactions at multiple redox-active sites during cell cycling.[18] The capacity retention results at different rates are shown in Fig. 2b and 2d. The Zn/HATAQ cells can undergo redox processes at current densities as high as 20 A g^{-1} and are remarkably stable for over 1000 cycles. Reversible specific capacities of 230, 231, 248, 238 and 199 mAh g^{-1} can be delivered, resulting in retention values of 70.1, 70.5, 90.0, 100.8 and 99.0 % after 1000 cycles for 2, 5, 10, 15 and 20 A g^{-1}, respectively, providing power density as high as 13.8 kW kg^{-1} at 20 A g^{-1}. The electrochemical performance was also investigated in terms of the rate capabilities (Fig. 2e). When the loading current is varied from 0.05 to 12 A g^{-1}, a highly reversible rate capability curve is obtained. Moreover, a capacity retention of 96.1 % was observed when the rate of 0.05 A g^{-1} was reapplied to the cell. This reveals excellent charge transfer kinetics of aqueous electrolyte. To our knowledge, such high capacity and excellent rate performance in HATAQ has rarely been observed in AZIBs (Fig. 2c). It is worth noting, however, that during preparation of this article, a study[19] reporting the performance of our HATAQ electrode[5] in AZIBs was published, further confirming our results on the excellent electrochemical performance of this material.

The highly reversible nature of the redox processes in HATAQ as seen in the electrochemical tests was confirmed by ex-situ Fourier-transform infrared (FT-IR) and Raman spectroscopy (Fig. S11-S13). Scanning electron microscopy (SEM) was used to investigate the nature of the HATAQ electrodes during cell cycling. Fig. 3a and 3b show SEM images of the pristine and discharged electrodes (0.2 V). The latter reveals the presence of zinc hydroxide sulfate (ZHS) with flake-like morphology on the electrode surface.[18-21] Scanning transmission electron microscopy (STEM) and energy dispersive X-ray spectroscopy (EDS) analyses were used to perform elemental

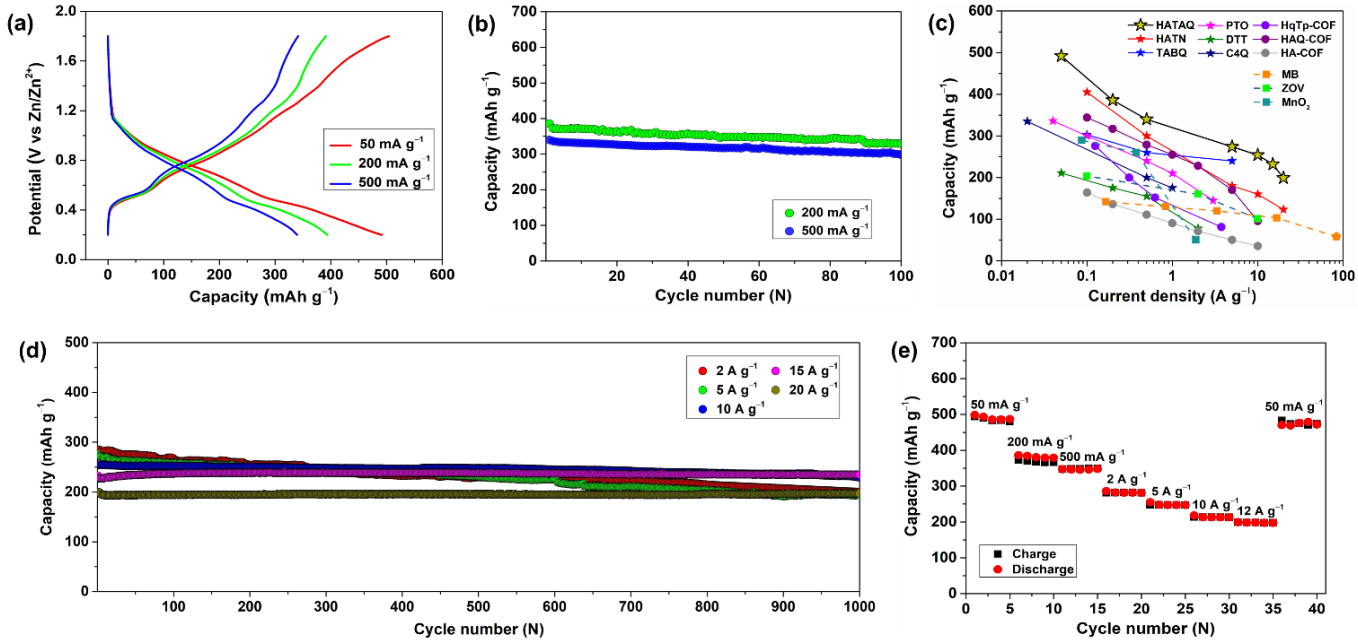

Fig. 2 (a) Galvanostatic voltage profiles of HATAQ electrodes at current densities ranging from 50 mA g^{-1} to 500 mA g^{-1}. (b) and (d) Capacity retention at different rates up to 20 A g^{-1}. (c) Capacity vs current density plot comparing HATAQ with small-molecule organic-based (star), polymeric organic-based (circle) and inorganic-based materials (square) recently reported as cathodes for AZIBs (HATN,[18] TABQ,[21] PTO,[23] DTT,[24] C4Q,[25] HqTp-COF,[26] HAQ-COF,[1] HA-COF,[1] MB,[27] ZOV[28] and MnO_2).[29] (e) Rate capability at various current densities.

mapping of HATAQ in pristine state and at the end of discharge (0.2 V) as shown in Fig. S14. It was found that C, N and O are dispersed uniformly over the whole particle of the pristine material with no presence of S or Zn, while in the case of discharged electrode, C and N signals are no longer visible with only O, S and Zn present. This suggests that during discharge ZHS will form and cover the whole surface of the HATAQ electrode.[6] ZHS formation is also seen in ex-situ PXRD profiles (Fig. 3c) carried out on electrodes at different voltage positions during discharge/charge processes. When the patterns from pristine electrode (dry) and electrode soaked in the electrolyte (wet) are compared with those discharged or charged, it is obvious that there is a new phase forming during discharge (indicated by *). The new peaks gradually become stronger during discharge and weaker during charge, which corresponds to the reversible formation of ZHS, $Zn_4(OH)_6SO_4{\cdot}xH_2O$, where x = 0, 0.5, 1, 3, 4 and 5 (Fig. S16-S19, Table S1, see ESI† for details).[6,20,22] It is also worth noting that the peak at ~27° corresponding to diffraction from the (006) plane, which is the layer stacking direction of HATAQ 2D arrangement,[5] remains visible throughout cycling, suggesting that the 2D layered structure is preserved during charge/discharge cycles. The PDFs in Fig. 3d also point to the formation of ZHS, which overlaps with the HATAQ signal in the discharged electrode. However, it can be seen that the peak at 4.25 Å corresponding to the in-plane C-C distances in HATAQ retains both in the pristine and discharged HATAQ, confirming the cycling stability of the cathode.

The PXRD/STEM-EDS data and computational results (Fig. S20, S21) indicate proton insertion mechanism of charge storage in the cathode, causing the structural evolution of the pristine HATAQ to HATAQ-12H. Consistent with previous studies of AZIBs,[18,21] reversible formation of ZHS (Fig. 3c) functions as a pH buffer for the system.[6,21] 1 M $ZnSO_4$ electrolyte has ~10^{-5} M of H^+ (pH ~4.5) together with the unlimited supply of H^+ at the electrode surface from dissociation of

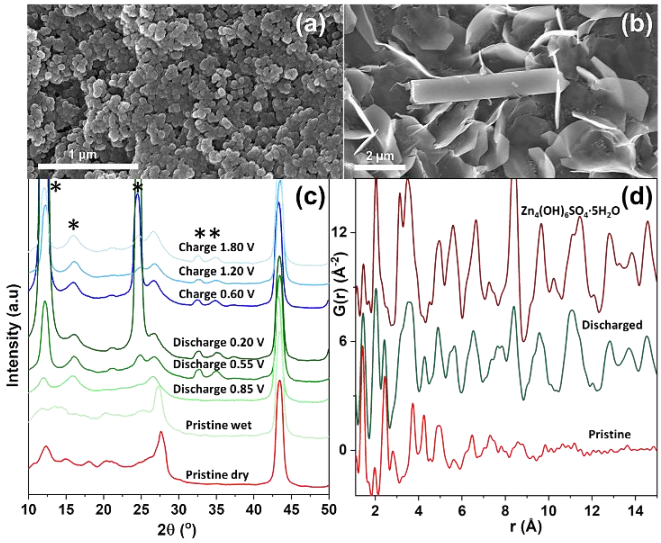

Fig. 3. (a) and (b) SEM images of HATAQ electrodes at pristine condition and at the end of discharge, respectively, showing the formation of flake-like zinc hydroxide sulfate (ZHS) on the electrode surface. (c) Ex-situ PXRD patterns of HATAQ electrodes at different discharge/charge states compared to those at pristine conditions (1 M $ZnSO_4$ aqueous electrolyte; 200 mA g^{-1}). The peak at 44° is from the stainless-steel mesh current collector (* indicates peaks from ZHS). (d) PDFs of the pristine HATAQ, discharged electrode and $Zn_4(OH)_6SO_4{\cdot}5H_2O$.

H_2O (promoted by the equilibrium of hydrated Zn^{2+} species) accompanied by the precipitation of ZHS.[6,21,24] To gain atomic-level insights into the HATAQ structural changes upon discharging, we have performed quantum mechanical calculations coupled with natural bond orbital (NBO) analysis.[30] Fig. 4a shows the characteristic C-H···O hydrogen bonding interactions in HATAQ, resulting from mixing of the carbonyl *s*-type n^{σ} lone pair with the σ* orbital of the

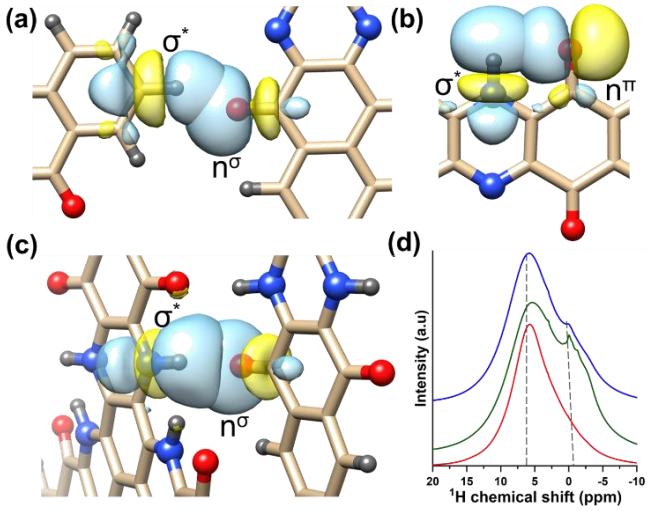

Fig. 4 (a) C-H···O (in-plane) intermolecular hydrogen bond in the pristine HATAQ. (b) N-H···O intramolecular C5 hydrogen bond in HATAQ-H. (c) N-H···O interlayer hydrogen bond in HATAQ-6H. The hydrogen bonds are characterized by the respective overlaps of the s-/p-type (n^{σ}/n^{π}) carbonyl lone pair and C-H/N-H (σ*) orbital. (d) ^{1}H solid-state NMR spectra of the pristine (red), discharged (green) and charged (blue) HATAQ electrodes.

C-H bond. As mentioned, these intermolecular hydrogen bonds help stabilize 2D arrangement of HATAQ molecules in the material, with the NBO estimated strength of 5.1 kcal mol^{-1}. Interestingly, upon the first proton intercalation we found the putative C5 hydrogen bond[31] in HATAQ-H (Fig. 4b), formed by overlap of the *p*-type n^{π} carbonyl lone pair with the N-H σ* orbital. Although 3.6 kcal mol^{-1} weaker than C-H···O, these intramolecular interactions were found to be important in the stabilization of proteins.[32] In the HATAQ-H, the appearance of the C5 hydrogen bond is more energetically favorable over possible O-H···N intramolecular interaction (Fig. S22). What may at first seem counterintuitive, this can be explained by the formation of the resonance stabilized vinylogous amide group in HATAQ-H (Fig. S23), when the protonation takes place at the imine nitrogen. Subsequent proton insertion steps go through the imine nitrogens towards maximazing the number of the vinylogous amides (Fig. S20). The intercalation of the sixth proton (HATAQ-6H) leads to the formation of strong (10.4 kcal mol^{-1}) inter-layer N-H···O hydrogen bonds (Fig. 4c) typically found between the peptide group carbonyl and N-H bonds in proteins. Thus, we speculate that weak C5 local contacts formed in the beginning of the discharge process could prepare HATAQ for association into more complex hydrogen bond network system, making the proton transfer possible within and across the 2D layers.

The H^+ insertion/extraction processes in bulk HATAQ can be further confirmed experimentally by ex-situ ^{1}H solid-state nuclear magnetic resonance (NMR) as shown in Fig. 4d. The NMR spectrum of pristine HATAQ shows a broad peak centered at ~6.0 ppm, which belongs to the H of benzene ring with two different chemical environments.[18] During discharge, a new peak emerges at ~0 ppm which can be ascribed to H in –NH–, supporting H^+ reaction with the redox centers of HATAQ,[18] which is in agreement with the computational results. Additionally, proton conduction and charge transfer processes were investigated using galvanostatic intermittent titration technique and electrochemical impedance spectroscopy measurements, respectively, (Fig. S24, S25). The obtained low activation energies below 340 meV suggest a facile proton transfer likely via the Grotthuss mechanism (activation energy reported to be below 400 meV),[21,33] where the proton transfer takes place through the transient hydrogen bonds (Fig. 4) between adjacent redox-active functional groups in HATAQ. CV measurements in Fig. S26 also indicate the domination of non-diffusion-controlled charge storage process and facile redox kinetics,[21,33] enabling an excellent rate performance of HATAQ cathode.

To further elucidate the mechanistic aspects of proton insertion in HATAQ electrode upon cycling, we performed isotopic substitution using three electrolytes at different cycling rates. As shown in Fig. S27, at the rate of 500 mA g^{-1}, the capacity values from 1 M $ZnSO_4/H_2O$ and 1 M $ZnSO_4/D_2O$ systems are almost identical. Upon the increase of cycling rate, the difference between the performances markedly increases from ~282 and 260 mAh g^{-1} to 212 and 137 mAh g^{-1}, respectively. This could be explained by taking into account that H^+ diffusion in H_2O is ~1.42 times faster than D^+ diffusion in D_2O,[34] and that at high rates ion diffusion could become capacity limiting step due to low H^+ and D^+ production rate in zinc-based electrolytes, electrode polarization and ZHS formation.[6,21]

Conclusions

We have applied nature-inspired strategy to develop high-performance small molecule HATAQ cathode in AZIBs. Surprisingly, it was found that similarly to protein stabilization in nature, the unique interplay between weak and strong hydrogen bonding interactions stabilizes the material structure, creating plausible trajectories for very fast proton conduction. Our studies strongly point to the importance of this biomimetic mechanism on the cathode performance, enabling HATAQ to achieve a capacity of 492 mAh g^{-1} at 50 mA g^{-1} and a reversible capacity of 199 mAh g^{-1} at an ultrahigh rate of 20 A g^{-1} with exceptional stability over 1000 cycles, which are found to be one of the highest in AZIBs reported to date (Table S2). The presented stabilization strategy is versatile and, given the synthetic tunability of OSMCs, can be adapted to modulate properties of electroactive materials in battery technologies.

Experimental

General methods and materials

Starting materials and solvents were purchased and used without further purification from commercial suppliers (Sigma-Aldrich and Alfa Aesar). The compound HATAQ was prepared by a reaction between 2,3-diamino-1,4-naphtaquinone and cyclohexane hexaketone according to our original procedure reported previously. PXRD patterns were collected on Bruker D8 Advance ECO. FT-IR spectra were recorded on Nicolet iS5 or Nicolet 6700, Thermo Scientific. The Raman spectra of the

samples were collected by UniDRON Raman microscope with an excitation laser beam wavelength of 633 nm. XPS measurements were performed on ULVAC PHI 5000 VersaProbe Ⅲ with Al Kα (1487 eV) as an X-ray source. Survey scans were collected with a pass energy of 100 eV, followed by high-resolution scans of the C 1s, N 1s and O 1s regions with a pass energy of 20 eV. All spectra were charge-corrected relative to the C 1s component at 284.5 eV binding energy and analyzed using CasaXPS software. SEM images were collected on a SU8010 HR-FESEM scanning electron microscope. STEM and EDS were carried out on JEOL JEM-2010 electron microscope. The ^{1}H solid-state NMR spectra were recorded on a Bruker Avance III HD 400MHz NMR.

Electrochemical studies

To prepare electrodes, HATAQ (30 wt%), Ketjen black conductive carbon (60 wt%), and poly(vinylidenedifluoride) (PVDF) (10 wt%) were mixed and ground in the presence of *N*-methyl-2-pyrrolidinone (NMP). The mass loading of the active material was kept at ~0.7 mg (for 30 wt%). Other ratios of electrode mixture, 45:45:10 and 60:30:10, were also tested. The slurry was coated onto carbon paper (MGL280) current collector and dried overnight at 100 °C in vacuum. CR2032 coin cells were assembled by using Zn metal as anode, 1 M $ZnSO_4$ aqueous solution as electrolyte and Whatman glass microfiber (GF/A) membrane as separator. Other Zn electrolytes (1 M $Zn(CF_3SO_3)_2$ in various solvent systems) were investigated to determine an optimized electrochemical performance. In addition, three-electrode cells with activated carbon (counter electrode), saturated calomel electrode (reference electrode) and HATAQ (working electrode) were employed to investigate the charge storage mechanism in three different electrolyte systems, 1 M $ZnSO_4$ in H_2O, 1 M H_2SO_4 in H_2O and 1 M $ZnSO_4$ in D_2O. The galvanostatic charge/discharge and CV measurements were carried out with a Neware battery cycler and a VMP3 system (BioLogic). Galvanostatic intermittent titration technique (GITT) was performed at current density of 80 mA g^{-1} for 15 min followed by a 2 h relaxation. Electrochemical impedance spectroscopy (EIS) measurements were carried out over a frequency range of 1 kHz−1 mHz. The coin cells were allowed to rest for at least 30 min before measurements. For activation energy calculations, the cells were placed in a temperature chamber and EIS and GITT data were collected at 35, 40, 45 and 50 °C. The cells were allowed to equilibrate for at least 1 h at each temperature.

Mechanistic studies

For all ex-situ analyses, the cells were cycled to various states of charge with a rate of 200 mA g^{-1}. The HATAQ electrodes for ex-situ Raman and FT-IR measurements contained 70 wt% active material, 20 wt% copper and 10 wt% PVDF.[35] The ex-situ XPS, PXRD and STEM-EDS were done on HATAQ electrodes consisting of 70 wt% active material, 20 wt% Ketjen Black and 10 wt% PVDF. Stainless steel was used as current collector for all these ex-situ experiments mentioned above. The coated electrodes were dried overnight at 100 °C in vacuum. For ex-situ SEM, the electrode mixture was prepared by using 30 wt% active material, 60 wt% Ketjen black and 10 wt% PVDF and coated onto carbon paper MGL280. The self-standing electrodes (0.2 mm thick) for ex-situ ^{1}H solid-state NMR contained 30 wt% active material, 60 wt% copper and 10 wt% poly(tetrafluoroethylene) (PTFE). The electrode mixture was combined together by using ethanol and the electrodes were dried in vacuum overnight at 80 °C. The coin cells were assembled by using Zn metal as anode, 1 M $ZnSO_4$ aqueous solution as electrolyte and Whatman glass microfiber (GF/A) membrane as separator. For all the ex-situ measurements, the electrodes were cycled to various states of charge and the cells were disassembled. Unless otherwise noted, the electrodes were washed with DI water and dried in vacuum at 80 °C for 24 h prior to ex-situ measurements. To remove the ZHS from the surface, each electrode was washed by soaking in acetic acid for 10 s, followed by rinsing with DI water and drying in vacuum at 80 °C. Additional details on the computational and synchrotron x-ray scattering measurements are provided in the ESI†.

Author contributions

N. T. H. L. performed all the electrochemical and mechanistic studies, with intellectual input from W. K., T.-H. C. and I. P. A. S. I. performed and analysed the computational and synchrotron x-ray scattering studies. I. P. synthesized the compound HATAQ. J.-C. L. conducted the XPS experiments. W. K., A. S. I. and I. P. interpreted the experiments and wrote the manuscript, incorporating the input from all the other authors.

Conflicts of interest

Provisional patent “Cathode Material of Aqueous Zinc-Ion Battery and Aqueous Zinc-Ion Battery” has been filed by the T.-H.C., W.K., N.T.H.L. and National Cheng Kung University (NCKU). Taiwan Application No. 110143424, 22 November 2021.

Acknowledgements

This work was supported by the Ministry of Science and Technology (MOST) of Taiwan under grant MOST109-2113-M-006-016 (to T.-H. C.) and the Young Scholar Fellowship Program MOST109-2636-E-006-001 (to W. K.). This work was also financially supported by the Hierarchical Green-Energy Materials (Hi-GEM) Research Center, from the Featured Areas Research Center Program within the framework of the Higher Education Sprout Project by the Ministry of Education (MOE) and MOST (MOST 109-2634-F-006-020) in Taiwan (to W. K.). This research was supported in part by High Education Sprout Project, Ministry of Education of the Headquarters of University Advancement at NCKU (to T.-H. C. and W. K.). The computational and scattering work by A. S. I. at ORNL was supported as part of the Fluid Interface Reactions, Structures and Transport (FIRST) Center, an Energy Frontier Research Center funded by the U.S. Department of Energy, Office of Science and Office of Basic Energy Sciences. ORNL is managed by UT-Battelle LLC for DOE under Contract No. DE-AC05-

00OR22725. I.P. was supported by the U.S. Department of Energy (DOE), Office of Science, Office of Basic Energy Sciences, Materials Sciences and Engineering Division under contract number DE-AC05-00OR22725. The 28-ID-1 beamline of the National Synchrotron Light Source II was used, which is a U.S. DOE Office of Science User Facility operated for the DOE Office of Science by Brookhaven National Laboratory under contract number DE-SC0012704. This research used resources of the Computer and Data Environment for Science (CADES) at Oak Ridge National Laboratory. The authors acknowledge the use of ESCA000200, NMR000700, NMR000800 and EM000800 of MOST 110-2731-M-006-001 belonging to the Core Facility Center of NCKU.

Notes and references

1 W. Wang, V. S. Kale, Z. Cao, Y. Lei, S. Kandambeth, G. Zou, Y. Zhu, E. Abouhamad, O. Shekhah and L. Cavallo, *Adv. Mater.*, 2021, **33**, 2103617.
2 Z. Tie and Z. Niu, *Angew. Chem. Int. Ed.*, 2020, **59**, 21293−21303.
3 W. Kaveevivitchai and A. Manthiram, *J. Mater. Chem. A*, 2016, **4**, 18737−18741.
4 T. B. Schon, B. T. McAllister, P.-F. Li and D. S. Seferos, *Chem. Soc. Rev.*, 2016, **45**, 6345−6404.
5 M.-S. Wu, N. T. H. Luu, T.-H. Chen, H. Lyu, T.-W. Huang, S. Dai, X.-G. Sun, A. S. Ivanov, J.-C. Lee, I. Popovs and W. Kaveevivitchai, *Adv. Energy Mater.*, 2021, **11**, 2100330.
6 M. Na, Y. Oh and H. R. Byon, *Chem. Mater.*, 2020, **32**, 6990−6997.
7 J. J. Shea and C. Luo, *ACS Appl. Mater. Interfaces*, 2020, **12**, 5361−5380.
8 A. Jouhara, N. Dupré, A.-C. Gaillot, D. Guyomard, F. Dolhem and P. Poizot, *Nat. Commun.*, 2018, **9**, 4401.
9 M. Kolek, F. Otteny, P. Schmidt, C. Mück-Lichtenfeld, C. Einholz, J. Becking, E. Schleicher, M. Winter, P. Bieker and B. Esser, *Energy Environ. Sci.*, 2017, **10**, 2334−2341.
10 Y. Liang and Y. Yao, *Joule*, 2018, **2**, 1690−1706.
11 J. Weng, Q. Xi, X. Zeng, Z.-Q. Lin, J. Zhao, L. Zhang and W. Huang, *Catal. Today*, 2021, DOI: 10.1016/j.cattod.2021.1009.1040.
12 K. A. Dill, *Biochemistry*, 1990, **29**, 7133−7155.
13 D. Bordo and P. Argos, *J. Mol. Biol.*, 1994, **243**, 504−519.
14 W. W. Cleland and M. M. Kreevoy, *Science*, 1994, **264**, 1887−1890.
15 Z. S. Derewenda, L. Lee and U. Derewenda, *J. Mol. Biol.*, 1995, **252**, 248−262.
16 V. Petkov, R. G. Difrancesco, S. J. L. Billinge, M. Acharya and H. C. Foley, *Philos. Mag. B*, 1999, **79**, 1519−1530.
17 R. Wyckoff, Crystal Structures (New York:Wiley). 1954.
18 Z. Tie, L. Liu, S. Deng, D. Zhao and Z. Niu, *Angew. Chem. Int. Ed.*, 2020, **59**, 4920−4924.
19 Y. Chen, J. Li, Q. Zhu, K. Fan, Y. Cao, G. Zhang, C. Zhang, Y. Gao, J. Zou, T. Zhai and C. Wang, *Angew. Chem. Int. Ed.*, 2022, DOI: 10.1002/anie.202116289.
20 B. Lee, H. R. Seo, H. R. Lee, C. S. Yoon, J. H. Kim, K. Y. Chung, B. W. Cho and S. H. Oh, *ChemSusChem*, 2016, **9**, 2948−2956.
21 Z. Lin, H.-Y. Shi, L. Lin, X. Yang, W. Wu and X. Sun, *Nat. Commun.*, 2021, **12**, 4424.
22 B. Sambandam, V. Soundharrajan, S. Kim, M. H. Alfaruqi, J. Jo, S. Kim, V. Mathew, Y.-k. Sun and J. Kim, *J. Mater. Chem. A*, 2018, **6**, 3850−3856.
23 Z. Guo, Y. Ma, X. Dong, J. Huang, Y. Wang and Y. Xia, *Angew. Chem. Int. Ed.*, 2018, **57**, 11737−11741.
24 Y. Wang, C. Wang, Z. Ni, Y. Gu, B. Wang, Z. Guo, Z. Wang, D. Bin, J. Ma and Y. Wang, *Adv. Mater.*, 2020, **32**, 2000338.
25 Q. Zhao, W. Huang, Z. Luo, L. Liu, Y. Lu, Y. Li, L. Li, J. Hu, H. Ma and J. Chen, *Sci. Adv.*, 2018, **4**, eaao1761.
26 A. Khayum, M. Ghosh, V. Vijayakumar, A. Halder, M. Nurhuda, S. Kumar, M. Addicoat, S. Kurungot and R. Banerjee, *Chem. Sci.*, 2019, **10**, 8889−8894.
27 M. Tang, Q. Zhu, P. Hu, L. Jiang, R. Liu, J. Wang, L. Cheng, X. Zhang, W. Chen and H. Wang, *Adv. Funct. Mater.*, 2021, **31**, 2102011.
28 D. Chao, C. Zhu, M. Song, P. Liang, X. Zhang, N. H. Tiep, H. Zhao, J. Wang, R. Wang and H. Zhang, *Adv. Mater.*, 2018, **30**, 1803181.
29 Y. Jin, L. Zou, L. Liu, M. H. Engelhard, R. L. Patel, Z. Nie, K. S. Han, Y. Shao, C. Wang and J. Zhu, *Adv. Mater.*, 2019, **31**, 1900567.
30 J. P. Foster and F. Weinhold, *J. Am. Chem. Soc.*, 1980, **102**, 7211−7218.
31 C. Toniolo, *CRC Crit Rev Biochem.*, 1980, **9**, 1−44.
32 R. W. Newberry and R. T. Raines, *Nat. Chem. Biol.*, 2016, **12**, 1084−1088.
33 X. Wu, J. J. Hong, W. Shin, L. Ma, T. Liu, X. Bi, Y. Yuan, Y. Qi, T. W. Surta, W. Huang, J. Neuefeind, T. Wu, P. A. Greaney, J. Lu and X. Ji, *Nat. Energy*, 2019, **4**, 123−130.
34 N. K. Roberts and H. L. Northey, *J. Chem. Soc., Faraday Trans. 1*, 1974, **70**, 253−262.
35 S. Wu, W. Wang, M. Li, L. Cao, F. Lyu, M. Yang, Z. Wang, Y. Shi, B. Nan, S. Yu, Z. Sun, Y. Liu and Z. Lu, *Nat. Commun.*, 2016, **7**, 13318.

